# Simulation and inversion of ultrasonic pitch-catch through-tubing well logging with an array of receivers

Erlend Magnus Viggen[a,*], Tonni Franke Johansen[a], Ioan-Alexandru Merciu[b]

[a] *SINTEF ICT, Acoustics Research Centre, Trondheim, Norway*
[b] *Statoil ASA, Research and Technology, Rotvoll, Norway*

---

**Abstract**

Current methods for ultrasonic pitch-catch well logging use two receivers to log the bonded material outside a single casing. For two casings separated by a fluid, we find by simulation that increasing the number of receivers provides a better picture of the effect of the bonded material outside the second casing. Inverting simulated measurements with five receivers, using a simulated annealing algorithm and a simple forward model, we find for a subset of simulations that we can estimate the impedance of the material outside the second casing.
*Keywords:* well logging, ultrasonic pitch-catch measurement, finite element simulation, mathematical modelling, inversion

---

## 1. Introduction

Multiple-casing well logging is a topic of increasing importance, in particular due to the large number of upcoming plug & abandonment operations [1]. Though very little has been published so far on ultrasonic logging in multiple-casing wells [1], ultrasonic logging in single-casing wells has been extensively studied [2, 3, 4, 5]. Current methods for single-casing pitch-catch well logging use two receivers, as this is sufficient to measure the exponential attenuation of the primary Lamb wave packet excited on the inner casing. This attenuation can be used to determine the impedance of the bonded material outside the casing [3, 4, 5].

In a double-casing geometry as shown in Figure 1, it has been found [1] that there appears a cascade of leaky Lamb wave packets between the two casings, where later packets feed on earlier ones. The amplitudes of the wave packets and the wavefronts that they emit are proportional. By measuring a wavefront's amplitude, the pitch-catch receivers $R_i$ can thus indirectly measure the relative amplitude of the corresponding wave packet at the time when it emitted the measured

*Corresponding author
*Email address:* `erlendmagnus.viggen@sintef.no` (Erlend Magnus Viggen)

Table 1: P-wave speed $c_\mathrm{p}$, density $\rho$, impedance $Z$, and s-wave speed $c_\mathrm{s}$ of simulated materials, taken from [1].

| **Material** | $c_\mathrm{p}$ [m/s] | $\rho$ [kg/m$^3$] | $Z$ [MRayl] | $c_\mathrm{s}$ [m/s] |
|---|---|---|---|---|
| Scree | 300 | 1700 | 0.51 | 0 |
| Water | 1481 | 1000 | 1.48 | 0 |
| Sat. shales & clays | 1200 | 2050 | 2.46 | 0 |
| Foam cement | 2250 | 1330 | 2.99 | 767 |
| Sat. shales & sand sect. | 1750 | 2150 | 3.76 | 336 |
| Chalk | 2400 | 1900 | 4.56 | 897 |
| Marls | 2400 | 2200 | 5.28 | 897 |
| Poro. & sat. sandstn. | 2600 | 2300 | 5.98 | 1069 |
| Class G cement | 3700 | 1800 | 6.66 | 2017 |
| Formation | 4645 | 2200 | 10.2 | 2646 |
| Steel casing | 5780 | 7850 | 45.4 | 3190 |

part on the wavefront. It has been found [1] that the wave packet amplitudes continuously evolve according to the system geometry and material parameters such as the impedance $Z_\mathrm{B}$ of the bonded material in the B-annulus, and that this impedance affects the amplitudes measured by the receivers from later wavefronts.

From these considerations we believe that increasing the number of receivers will improve the possibility and accuracy of inversion to determine the system's parameters, as more points along the packets' evolution are then measured. In this letter we show and discuss results of finite element simulations with five receivers, and demonstrate the possibility of inversion in a subset of the simulated cases.

## 2. Simulation setup, results, and discussion

Finite element simulations were performed in the system's two-dimensional cross-section. The simulation setup, shown in Figure 1, is identical to that in [1], with the exception that five receivers are used instead of two. The receivers $\mathrm{R}_i$ are positioned 10 cm apart. The first receiver's face centre is 25 cm away from the transmitter's face centre. The number and position of the receivers has not been optimised, but was chosen as a simple extension of [1] with additional receivers that provide information on the later evolution of the wave packets while

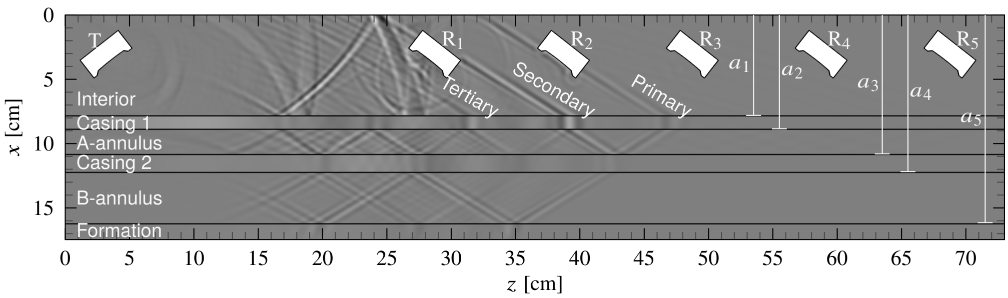


Figure 1: Snapshot of the simulated system at 170 µs with water in the interior and both annuli, showing pressure in the fluids and $x$-displacement in the solids

keeping tool size and computational requirements manageable. The inner casing has a diameter $2a_2 = 7$ in and a thickness $a_2 - a_1 = 0.408$ in, while the outer has a diameter $2a_4 = 9\frac{5}{8}$ in and a thickness $a_4 - a_3 = 0.545$ in.

As in [1], we restrict ourselves to a simple through-tubing case with water in the interior and the A-annulus, and a variety of materials from Table 1 in the B-annulus. To keep the model simple, and because attenuation is less important for pitch-catch logging except in oil-based muds with very high attenuation, all materials are assumed to be non-attenuating. We discuss the role of attenuation further in Sec. 3.

The simulation snapshot in Figure 1 shows the train of leaky Lamb wave packets on both casings, and the leaked wavefronts connecting these. The wavefronts emitted by the packets on the inner casing are measured by the receivers, which filter the impinging pressures and return nondimensionalised signals $S_{\mathrm{R}_i}(t)$. Because a wavefront's amplitude is proportional to its corresponding wave packet's amplitude at the time of emission, the received wavefront signals $S_{\mathrm{R}_i}(t)$ shown in Figure 2a tell of the wave packets' evolution. The peak amplitude corresponding to wavefront $k$ in the envelope of $S_{\mathrm{R}_i}(t)$ is denoted as $S_{\mathrm{R}_i,k}$.

In Figure 2a we see that the primary wavefront decreases exponentially, that the secondary wavefront peaks between $\mathrm{R}_1$ and $\mathrm{R}_2$, and that the tertiary wavefront decreases and increases in amplitude again from $\mathrm{R}_3$ to $\mathrm{R}_5$. As we will see in Sec. 3, these phenomenona can be understood through the model presented in [1], and simulated measurements can be used to determine the parameters of this model. With only two receivers as in [1], these phenomena would not have been captured, making it much less feasible determine the physical system from the measurements.

The evolution of the first few wavefronts for various B-annulus materials is shown in for the original geometry in Figure 2b and in Figure 2c for a modified geometry with equally thick

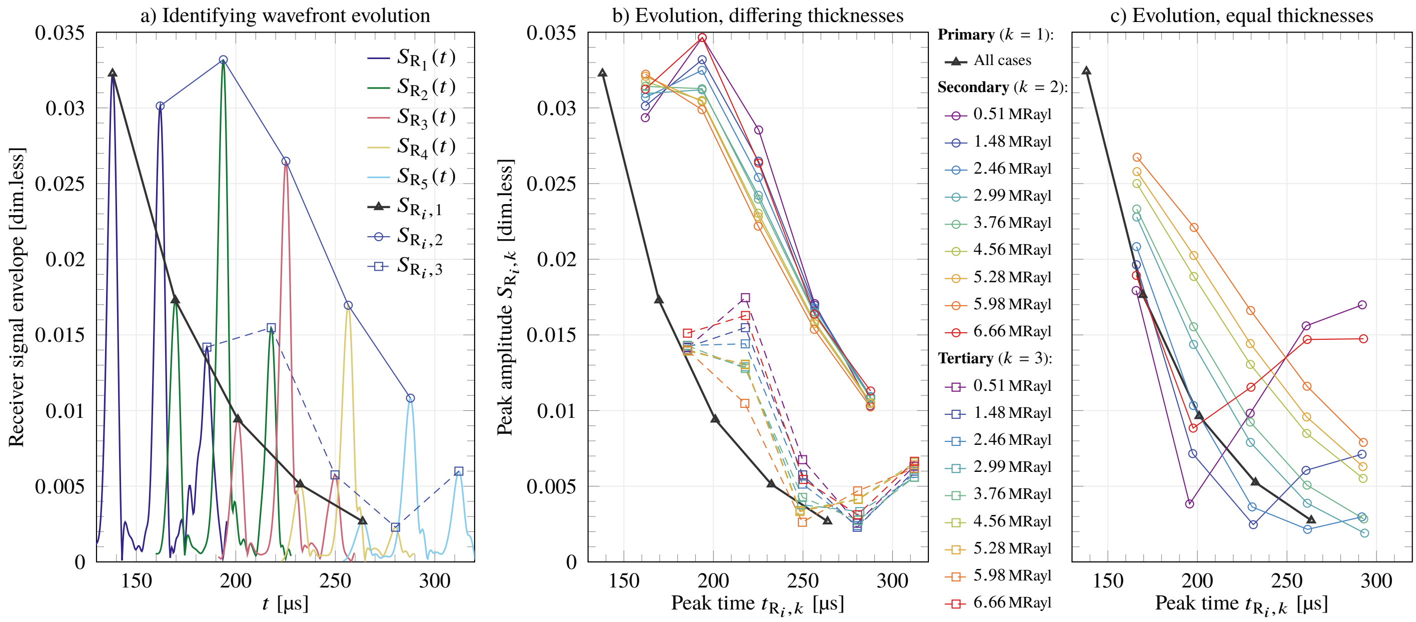


Figure 2: **a)** Envelopes of receiver signals $S_{\mathrm{R}_i}(t)$ for water (1.48 MRayl) in the interior and the annuli, along with indicated evolution of primary, secondary, and tertiary wavefronts. **b)** Evolution of primary, secondary, and tertiary wavefronts for original casing thicknesses and 9 different B-annulus materials from Table 1, as specified in the legend. **c)** Similarly, evolution of primary and secondary wavefronts for equal casing thicknesses.

casings ($a_4 - a_3 = 0.408$ in) where the dispersion relations on both casings are very similar. For the original geometry there is a smaller effect of material variation on the secondary and tertiary wavefront, and the same evolution pattern is seen for all materials. For equal casing thicknesses the variation is much stronger on both the secondary and tertiary wavefronts. (To keep Figure 2c readable, the latter are not shown.) Generally, this matches earlier observations of the outer annulus impedance $Z_\mathrm{B}$ having a larger effect with equal casing thicknesses, which may come from the dispersion relations on the casings being more similar so that the wave packets on both casings tend to stay in phase relative to each other [1]. Additionally, we see in both cases that the curves' behaviour is ordered by the B-annulus impedance with the exception of the highest-impedance material. The latter material behaves differently as its p-wave speed $c_\mathrm{p}$ is higher than the wave packet speed on the outer casing, which breaks the p-wave coupling [1, 3].

We define a logarithmic amplitude ratio, which for steady decay corresponds to attenuation in decibels per unit length, as

$$\alpha_{i,j,k} = \frac{20}{\Delta z_{i,j}} \log\left(\frac{S_{\mathrm{R}_i,k}}{S_{\mathrm{R}_j,k}}\right) \tag{1}$$

Here, $\Delta z_{i,j} = 10(j - i)$ cm is the distance between transducers $\mathrm{R}_i$ and $\mathrm{R}_j$. Only $\alpha_{1,2,1}$ and $\alpha_{1,2,2}$ have previously been examined against $Z_\mathrm{B}$ as only two transducers have been available [1]. A

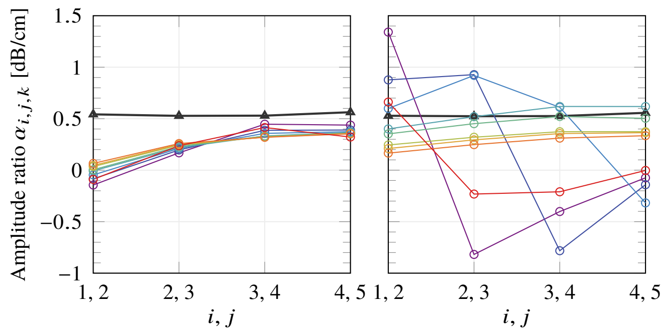


Figure 3: Amplitude ratios for primary and secondary wavefronts for 9 different B-annulus materials, using the same legend as the $S_{\mathrm{R}_i,k}$ plots in Figure 2. Left: Original casing thicknesses. Right: Equal casing thicknesses.

plot of amplitude ratios for adjacent receivers $\mathrm{R}_i$ and $\mathrm{R}_j = \mathrm{R}_{i+1}$ is shown for both thickness cases in Figure 3. We see that the primary wavefronts are in constant steady decay, and in most cases we see that the secondary wavefronts have also settled into steady decay by the 4th or 5th receiver. A preliminary 10-receiver simulation for original casing thicknesses and water in the outer annulus suggested that the tertiary wavefront similarly settles into steady decay by the 7th or 8th receiver.

As we could expect from Figure 2b, the differences in amplitude ratio are not large for the original casing thicknesses. However, in this case we also found that all amplitude ratios are ordered by impedance, except for the highest-impedance material which diverges as explained above. For equal casing thicknesses, the three fluids and the highest-impedance material have not reached steady decay by the 5th receiver, but the attenuations are ordered by impedance for the other materials.

## 3. Possibility of inversion

We may use inversion to determine the properties of the system from measured wavefront amplitudes, given that we have a forward model where a set of wavefront amplitudes may be calculated from a given set of system parameters, denoted as **a**. Several forward model alternatives are possible. Numerical simulations like those described above are relatively straightforward, but generally much too slow to be used for inversion. For this reason, faster semi-analytical forward models have been developed [2, 1], though the more general ones are by necessity very complex.

In this case we will apply a simple forward model designed to track the evolution of cascading Lamb wave packets on two parallel casings separated by a fluid [1]. As we are now measuring the wave packet amplitudes indirectly through their emitted wavefronts, we will adapt the model accordingly. Several assumptions underlie this forward model, most notably that the dispersion relations on both casings are sufficiently similar that the wave packets on both casings approximately remain in the same relative phase. We will therefore only apply this model in the subset of simulated cases for which it is appropriate, namely for equal casing thicknesses and B-annulus materials with p-wave coupling to the casing. Even so, this model will still let us test the principle of determining the impedance $Z_{\mathrm{B}}$ from the five receivers' measured wavefront amplitudes $S_{\mathrm{R}_i,k}$.

The model follows the time evolution of the signed amplitude $B_n(t)$ of each wave packet $n$. $n = 1, 3, 5$ corresponds to the primary, secondary, and tertiary wave packet on the inner casing, respectively; it is these wave packets' amplitudes that we can measure indirectly through their emitted wavefronts impinging on the receivers. Even values of $n$ correspond to wave packets on the outer casing, whose amplitudes cannot be measured by the receivers. The sign of $B_n(t)$ indicates whether wave packet $n$ is in phase or in counter-phase with respect to the primary packet $B_1(t)$.

Each wave packet is attenuated as it leaks wavefronts into the adjacent media. The attenuation rate is characterised by the decay constants $\lambda_{\mathrm{I}}$, $\lambda_{\mathrm{A}}$, and $\lambda_{\mathrm{B}}$, corresponding to the leakage into the interior, the A-annulus, and the B-annulus, respectively. For low impedances, these decay constants are proportional to the respective material impedances $Z_{\mathrm{I}}$, $Z_{\mathrm{A}}$, and $Z_{\mathrm{B}}$ [4]. The wavefronts' time of flight in the A-annulus between wave packets is denoted as $\Delta t$. When a wavefront in the A-annulus hits a casing, is is transmitted into the casing with a transmission coefficient $T$ and reflected with a reflection coefficient $R$. Thus, the evolution of each wave packet's signed amplitude $B_n(t)$ can be expressed through the ordinary differential equation

$$\frac{dB_n(t)}{dt} = T\lambda_{\mathrm{A}} \sum_{i=1}^{n-1} R^{n-(i+1)} B_i[t-(n-i)\Delta t] - \lambda_n B_n(t), \quad \text{with} \quad \lambda_n = \begin{cases} \lambda_{\mathrm{I}} + \lambda_{\mathrm{A}} & \text{for } n \text{ odd}, \\ \lambda_{\mathrm{A}} + \lambda_{\mathrm{B}} & \text{for } n \text{ even}. \end{cases} \tag{2}$$

Here, $\lambda_n$ is the total decay constant for wave packet $n$. The sum on the right-hand side corresponds to the total influence of earlier wave packets, while the second term corresponds to attenuation due to leakage. Applying appropriate initial conditions for the first wave packet, we find

$$CB_1(t) = CB_1(0)\, \mathrm{e}^{-(\lambda_{\mathrm{I}}+\lambda_{\mathrm{A}})t} H(t-t_0), \tag{3}$$

where $B_1(0)$ is the primary wave packet's amplitude extrapolated back to $t = 0$, $C$ is a constant

Table 2: Results of simulated annealing optimisation on the four lowest-impedance cases, with statistics based on 25 optimisation runs. The objective function from the set $\bar{\mathbf{a}}$ of mean parameters is also shown. Values of $\lambda_B$ and $f(\bar{\mathbf{a}})$ are shown for additional cases in Figure 5.

| **Parameter** | **0.51 MRayl** (fluid) | **1.48 MRayl** (fluid) | **2.46 MRayl** (fluid) | **2.99 MRayl** (solid) |
|---|---|---|---|---|
| $CB_1(0)$ | $0.514 \pm 0.033$ | $0.501 \pm 0.027$ | $0.451 \pm 0.024$ | $0.380 \pm 0.030$ |
| $t_0$ [μs] | $77.2 \pm 4.1$ | $71.9 \pm 4.6$ | $76.2 \pm 2.7$ | $67.3 \pm 4.4$ |
| $\Delta t$ [μs] | $20.6 \pm 0.8$ | $20.5 \pm 0.9$ | $19.9 \pm 0.7$ | $21.2 \pm 1.5$ |
| $T$ | $1.98 \pm 0.03$ | $1.83 \pm 0.05$ | $1.97 \pm 0.03$ | $1.87 \pm 0.09$ |
| $R$ | $-0.98 \pm 0.01$ | $-0.97 \pm 0.02$ | $-0.98 \pm 0.01$ | $-0.99 \pm 0.02$ |
| $\lambda_w$ [ms$^{-1}$] | $10.0 \pm 0.2$ | $9.9 \pm 0.1$ | $9.5 \pm 0.2$ | $9.0 \pm 0.2$ |
| $\lambda_B$ [ms$^{-1}$] | $4.5 \pm 0.5$ | $10.0 \pm 0.5$ | $15.1 \pm 0.3$ | $19.4 \pm 1.7$ |
| $f(\bar{\mathbf{a}})$ | $19.7 \times 10^{-4}$ | $12.4 \times 10^{-4}$ | $16.5 \times 10^{-4}$ | $33.0 \times 10^{-4}$ |

conversion factor from the wave packet amplitude to the wavefront amplitude measurable by the receivers, $t_0$ is the wavefronts' time in flight in the interior from transmitter to casing and from casing to receiver, and $H$ is the Heaviside function.

Some additional restrictions were imposed on the model parameters. In this through-tubing logging case with water in the interior and the A-annulus, we use a single decay constant for both, $\lambda_I = \lambda_A = \lambda_w$. Additionally, stability considerations imply $T + R \leq 1$ and $T < 2$ [1]. No further restrictions were used, though in practice it might be possible to use prior knowledge to determine or limit some additional parameters.

We apply this model to a case with non-attenuating materials, but attenuating materials would not be outside its scope. Attenuation in the B-annulus is not an issue as it would not affect the evolution of the wave packet amplitudes. As attenuation in the interior would affect each wavefront by the same factor it could be absorbed into the constant $C$. Attenuation in the A-annulus could be modelled by introducing a new parameter $D$ for the wavefront decay from one wave packet to the next, and would appear in Eq. 2 as a factor $D^{n-i}$ inside the sum. In practice, the attenuation in the interior and the A-annulus would reduce the signal-to-noise ratio of the receivers' measurements, but this is not an issue for this forward model.

To find optimised sets $\mathbf{a}$ of system parameters from the measured wavefront amplitudes $S_{R_i,k}$,

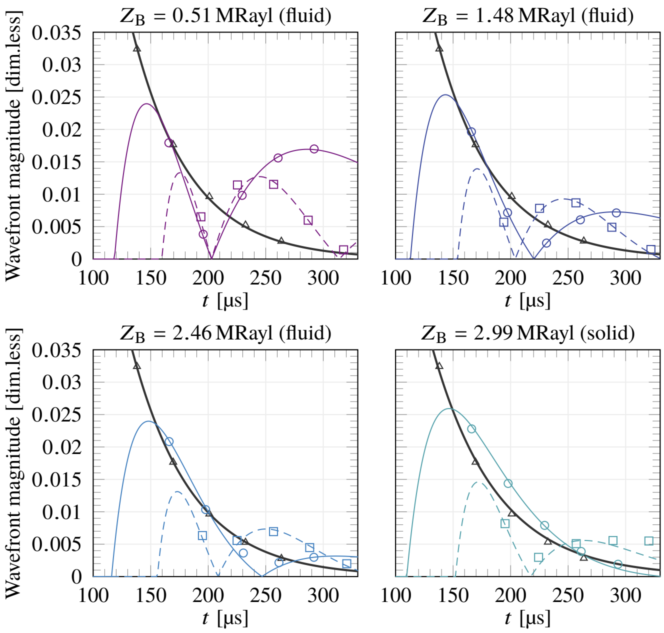


Figure 4: Optimised fits of simulated measurements $S_{\mathrm{R}_i,k}$ (marks) to modelled wavefront magnitudes $|CB_n(t)|$ (lines) for the primary (triangles, thick solid line), secondary (circles, solid line), and tertiary (squares, dashed line) wavefronts, using the sets $\bar{\mathbf{a}}$ of mean parameters from Table 2.

we used the stochastic optimisation method called simulated annealing. The objective function $f(\mathbf{a})$ was chosen as the $L_2$ norm of the deviation between modelled wavefront amplitudes and simulated measurements of these,

$$f(\mathbf{a}) = \sqrt{\sum_{i=1}^{5} \left[ (|CB_1(t_{\mathrm{R}_i,1})| - S_{\mathrm{R}_i,1})^2 + (|CB_3(t_{\mathrm{R}_i,2})| - S_{\mathrm{R}_i,2})^2 + (|CB_5(t_{\mathrm{R}_i,3})| - S_{\mathrm{R}_i,3})^2 \right]}, \quad (4)$$

with $B_n(t)$ determined from a parameter set $\mathbf{a}$. In other words, the model parameters were optimised to give a least-squares fit with the simulated measurements.

Due to the stochastic nature of simulated annealing, slightly different optimal parameter sets $\mathbf{a}$ are typically found from run to run. For this reason, Table 2 provides each resulting parameter for each of the four lowest-impedance cases as a mean value and a standard deviation, based on 25 well-converged runs. The start conditions for each case were chosen from preliminary runs; in all cases, the finally chosen start conditions fell within the determined standard deviation range. The fit between the measured wavefront peak amplitudes $S_{\mathrm{R}_i,k}$ and modelled wavefront magnitudes $|CB_n(t)|$ is shown in Figure 4.

From Table 2 and Figure 5 we find as expected that there is a near-linear correspondence between $\lambda_{\mathrm{B}}$ and $Z_{\mathrm{B}}$, especially for low impedances $Z_{\mathrm{B}}$ where the underlying assumptions of the forward model are most valid. We can also find that there is a fairly large variation in $t_0$,

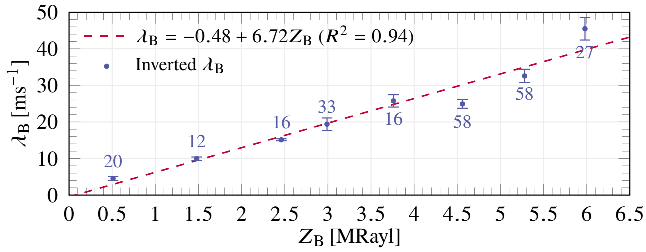


Figure 5: Linear fit of $\lambda_B$ against $Z_B$ for all but the highest-$c_p$ material which, as explained above, lacks p-wave coupling to the Lamb wave; its behaviour is therefore qualitatively different and it cannot be compared to the other materials [1, 3]. Also shown for each $\lambda_B$ are the objective function values $f(\bar{\mathbf{a}}) \times 10^4$, where lower values indicate more trustworthy results.

even though there should not be as $t_0$ is physically determined by the constant geometry and material in the interior. Figure 4 would suggest that the uncertainty in $t_0$ could be reduced by placing an additional receiver closer to the transducer to measure the rapid early evolution of the wavefronts; however, such measurements would be polluted by fluid-borne waves from the transmitter [1]. Similarly, there is a significant variation in $T$. In the fourth case, the higher value of $f(\bar{\mathbf{a}})$ indicates a significantly poorer fit between the simulated measurements and the model, suggesting that the model represents a poorer approximation for this higher-impedance material.

## 4. Conclusion

The wavefront amplitudes $S_{R_i,k}$ measured by the receivers in a pitch-catch setup are directly connected to the amplitude evolution of the leaky Lamb wave packets on the inner casing. This evolution depends on the system geometry and materials, including the impedance of the material bonded to the outer casing. With $n$ receivers, we may thus measure $n$ points along the evolution of each wave packet. Thus, with more receivers we can get a better picture of the wave packets' evolution and we can thus in principle determine the measured system's properties with greater accuracy. In this letter we have shown that using five receivers gives a clearer picture of the wave packet evolution than using two receivers [1].

Additionally, we were able to use a simple forward model to perform a limited inversion on a subset of simulated measurements, finding that the inverted model parameter $\lambda_B$ varied nearly linearly with the impedance $Z_B$. To be able to perform a more general inversion, we would need to apply a more general forward model that can deal with factors such as differing dispersion relations on the casings, casing eccentricity, misaligned casings, and attenuating fluids. Still, our findings indicate that the principle of determining the bonded material in the B-annulus from the measurements $S_{\mathrm{R}_i,k}$ is sound.

Future work could investigate improved receiver setups, using the same system as a test case. The physically embodied receivers in the simulations reported here could be replaced with an array of acoustically invisible receivers. While these receivers would not themselves be physically realisable, they would provide a closer sampling of the wavefronts, and by array signal processing of the signals from these receivers we could study different possibilities for improving physically realisable tools.

**Acknowledgements**

This work has been sponsored by Statoil. We acknowledge the aid of Statoil's Kevin Constable and Pål Hemmingsen.

**References**

[1] E. M. Viggen, T. F. Johansen, I.-A. Merciu, Simulation and modeling of ultrasonic pitch-catch through-tubing logging, Geophys. 81 (4) (2016) D369–D379. doi:10.1190/geo2015-0251.1.

[2] S. Zeroug, Analytical modeling for fast simulations of ultrasonic measurements on fluid-loaded layered elastic structures, IEEE Trans. Ultrason. Ferroelectr. & Freq. Control 47 (3) (2000) 565–574. doi:10.1109/58.842043.

[3] R. van Kuijk, S. Zeroug, B. Froelich, M. Allouche, S. Bose, D. Miller, J.-L. le Calvez, V. Schoepf, A. Pagnin, A novel ultrasonic cased-hole imager for enhanced cement evaluation, in: Internatl. Petro. Tech. Conf., 2005, p. 14. doi:10.2523/10546-MS.

[4] R. van Kuijk, J.-L. le Calvez, B. Froelich, Determination of the impedance of a material behind a casing combining two sets of ultrasonic measurements, U. S. Patent 7,149,146 B2 (2006).

[5] H. Wang, G. Tao, X. Shang, Understanding acoustic methods for cement bond logging, J. Acoust. Soc. Am. 139 (5) (2016) 2407–2416. doi:10.1121/1.4947511.